Letter

Magneto-Seebeck effect and ambipolar Nernst effect in the CsV₃Sb₅ superconductor

Yuhan Gan,[1,*] Wei Xia,[2,3,*] Long Zhang,[1,*] Kunya Yang,[1] Xinrun Mi,[1] Aifeng Wang,[1] Yisheng Chai ®,[1]
Yanfeng Guo ®,[2,†] Xiaoyuan Zhou,[1,‡] and Mingquan He ®[1,§]

[1]*Low Temperature Physics Lab, College of Physics & Center of Quantum Materials and Devices,
Chongqing University, Chongqing 401331, China*
[2]*School of Physical Science and Technology, ShanghaiTech University, Shanghai 201210, China*
[3]*ShanghaiTech Laboratory for Topological Physics, Shanghai 201210, China*

We present a study of Seebeck and Nernst effect in combination with magnetoresistance and Hall measurements of the Kagome superconductor CsV₃Sb₅. A sizable magneto-Seebeck signal appears once the charge density wave (CDW) order sets in below $T_{CDW} = 94$ K. The Nernst signal peaks at a lower temperature $T^* \sim 35$ K, crossing which the Hall coefficient switches sign, which we attribute to the ambipolar transport of compensated bands due to the multiband nature of CsV₃Sb₅. Sublinear Nernst signal and Hall resistivity also develop well below the CDW transition, which becomes apparent below T^*. These findings suggest that, the multiband electronic profile plays an important role in the transport properties of the CDW state in CsV₃Sb₅.

Intertwined orders, such as magnetic, charge, nematic and superconducting orders, often lead to rich phases in quantum materials [1]. Involvement of nontrivial band topology can further enrich the physics, as evidenced by the advent of magnetic topological materials [2], topological superconductors [3], etc. The recent discovered superconducting Kagome family AV₃Sb₅ (A = K, Rb, Cs) provides another prime example to investigate the interplay between intertwined orders and nontrivial band topology [4–7]. Various intriguing features, including charge density wave (CDW) [8–15], superconductivity [4–7], nematicity [16] and Dirac-like bands [4,5,17–22], have been identified in these compounds, which have triggered intensive research effort to unveil the nature of CDW and superconductivity, and to search for nontrivial states in this Kagome system [23].

Both density functional theory calculations and angle-resolved photoemission spectroscopy experiments have suggested a multiband electronic structure in AV₃Sb₅ [4,5,17–22,24,25]. An electron pocket is located at Brillouin zone (BZ) center (Γ point), involving the p_z orbital of in-plane Sb atoms. The d orbitals of V atoms intersect with the Fermi level at the BZ boundaries, forming both electron ($k_z = \pi$, L point) and hole ($k_z = 0$) bands at the M point [17]. Additionally, two Van Hove singularity points (saddle points) pop up near the Fermi level around the M point. The CDW phase emerges in all three systems below $T_{CDW} \sim 80$–100 K [4–7]. Consequently, substantial Fermi surface reconstruction occurs mainly on the pockets at the M point, which is accompanied by moderate lattice distortions [21].

The multiband electronic structure also complicates the transport properties. Intriguingly, a giant anomalous Hall effect (AHE) has been reported in the CDW phase of K_{1-x}V₃Sb₅ [26] and CsV₃Sb₅ [27,28], despite the absence of long-range magnetic order [4]. The origin of the observed giant AHE is still a mystery, which was initially attributed to extrinsic skew scattering of spin clusters [26]. Transport experiments on gate-tuned thin flakes of CsV₃Sb₅ also suggest dominant contribution from extrinsic skew scattering of ferromagnetic fluctuations [28]. On the other hand, muon spin spectroscopy (μSR) experiments found negligible local moments, suggesting a subdominant role played by spin clusters [29]. Nevertheless, recent μSR measurements revealed an enhanced local magnetic field inside the CDW phase [30,31], pointing to the emergent time reversal symmetry breaking effect, which may be another prominent source of AHE [32]. Despite various scenarios, the impacts of multi-band transport remain less explored, and the transport study is hitherto limited to the resistivity channel. Here, we present Seebeck and Nernst measurements on single crystalline CsV₃Sb₅. Sign switching in the Seebeck channel, together with the nonlinear Hall and Nernst effects are observed well below the CDW transition, suggesting the important role played by multiband nature. More importantly, the Nernst signal peaks at $T^* \sim 35$ K, where the Hall coefficient also changes sign, which is a signature of ambipolar transport of compensated bands.

Single crystalline CsV₃Sb₅ samples were grown by the self-flux method as described elsewhere [33]. The Seebeck, Nernst, magnetoresistance, and Hall measurements were performed in a 14-T Oxford cryostat. Longitudinal resistivity and magnetoresistance were measured using the standard four-probe method. Hall measurements were performed using a five-terminal configuration. One heater, two-thermometer geometry was used to capture the thermopower and Nernst effect. Two Keithley 2182A nanovoltmeters were used to record the Seebeck and Nernst signals at the same time.
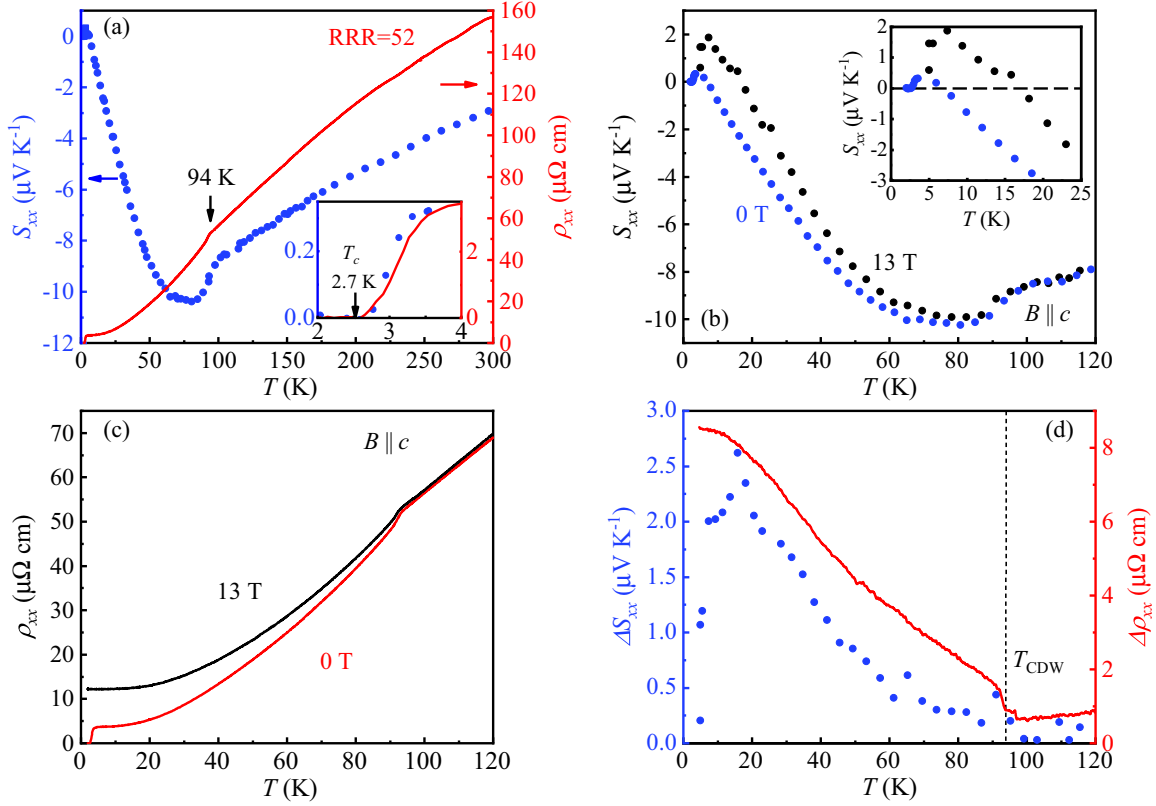
FIG. 1. (a) Temperature dependence of the in-plane Seebeck coefficient and resistivity. The residual resistivity ratio is RRR = $\rho_{xx}(300\,\text{K})/\rho_{xx}(5\,\text{K}) = 52$. (b), (c) Seebeck effect and resistivity measured in zero magnetic field and $B = 13$ T with field applied along the c-axis. (d) The magneto-Seebeck effect $\Delta S_{xx} = S_{xx}(13\,\text{T}) - S_{xx}(0\,\text{T})$ and magnetoresistance $\Delta\rho_{xx} = \rho_{xx}(13\,\text{T}) - \rho_{xx}(0\,\text{T})$ evaluated using the data shown in (b) and (c). The inset in (b) displays a zoomed in view in the vicinity of sign change in S_{xx}.

In Fig. 1, we present the in-plane Seebeck signal S_{xx}, and longitudinal resistivity ρ_{xx} of a CsV_3Sb_5 single crystal. The CDW transition is manifested by a kink at 94 K in resistivity, which is much more pronounced in thermopower [see Fig. 1(a)]. Followed by the sudden drop at T_{CDW}, the thermopower reaches a broad maximum around 70 K, which is likely a consequence of phonon drag contribution. The phonon drag peak typically appears around $\theta_D/5$ (θ_D: Debye temperature) in metals [34]. The Debye temperature is estimated to be $\theta_D = 204$ K for our CsV_3Sb_5 sample (see Fig. S2 in the Supplemental Material [35]). Superconductivity occurs below $T_c = 2.7$ K, characterized by zero resistance and zero thermopower [see the inset of Fig. 1(a)]. Both the CDW and superconducting transition temperatures match well with those reported earlier [5,27].

The Seebeck signal shows a negative sign at most temperatures measured here. This implies that the thermopower is dominated by electronlike carriers. Notably, a sign change occurs in $S_{xx}(T)$ around 7 K at zero field, which shifts to a higher temperature ~ 17 K in 13 T [see the inset of Fig. 1(b)]. The sign change in $S_{xx}(T)$ is likely a consequence of multiband transport. For a multiband system, the Seebeck signal S can be written as [34]

$$S = \frac{\sum \alpha_m}{\sum \sigma_m} = \frac{\sum \sigma_m S_m}{\sum \sigma_m} = \frac{\sum n_m e \mu_m S_m}{\sum n_m e \mu_m}, \quad (1)$$

where $\alpha_m = \sigma_m S_m$ is the thermoelectric (Peltier) conductivity of a band with index m, $\sigma_m = n_m e \mu_m$ is the electrical conductivity with carrier density n_m and mobility μ_m of the corresponding band, $e > 0$ is the elementary charge. In the simple free electron gas picture, and if the relaxation time is energy-independent, the contribution of each band S_m can be modeled by the Mott relation [36,37], $S_m = \pm \frac{\pi^2 k_B^2 T}{3e} \frac{N_m(E_F)}{n_m}$, where k_B is the Boltzman constant, $N_m(E_F)$ is the density of states (DOS) at the Fermi level, T is the Kelvin temperature, E_F is the Fermi energy. The plus (minus) sign is for hole (electron)-like band. The total Seebeck coefficient of a two-band system with an electronlike and a holelike band is then

$$S = \frac{\pi^2 k_B^2 T}{3e} \frac{e \mu_h N_h - e \mu_e N_e}{n_h e \mu_h + n_e e \mu_e}, \quad (2)$$

where $n_{e(h)}$, $\mu_{e(h)}$ and $N_{e(h)}$ represent the density, mobility and DOS of electron (hole) carriers, respectively. As shown in Fig. 3, although the electrical conductivity is dominated by holelike carriers below ~ 35 K with much higher concentration n_h, the mobility of the electronlike band μ_e is much larger, which gives the overall negative sign in the thermopower. The positive sign below 7 K suggests the dominant contribution from the holelike band with higher DOS N_h. The N_h is likely further enhanced by the application of magnetic field, which shifts the crossing point to higher temperatures.
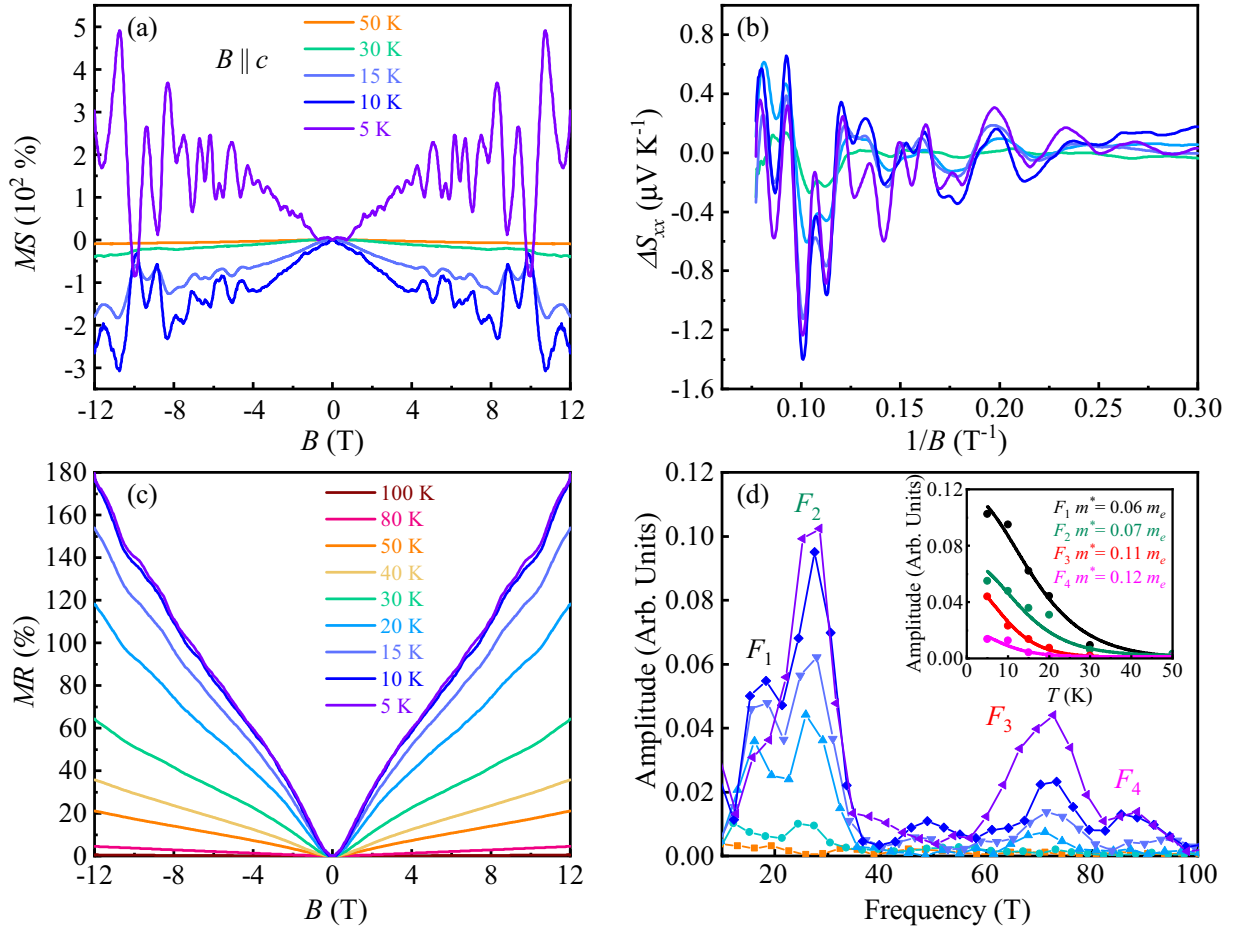
FIG. 2. (a) Magneto-Seebeck $MS = [S_{xx}(B) - S_{xx}(0)]/S_{xx}(0)$ and (c) magnetoresistance $MR = [\rho_{xx}(B) - \rho_{xx}(0)]/\rho_{xx}(0)$ measured at various temperatures with $B \parallel c$. (b) The quantum oscillations ΔS_{xx} plotted as a function of $1/B$. The data is obtained by subtracting a polynomial background between 2 and 12 T from the MS results shown in (a). (d) Extracted frequency from the FFT analysis of the oscillation data in (b). Four frequencies with $F_1 = 18$, $F_2 = 28$, $F_3 = 72$ and $F_4 = 88$ T are found. The inset shows the corresponding effective mass m^* estimated using the Lifshitz-Kosevich approach.

As shown in Figs. 1(b) and 1(c), sizable magneto-Seebeck and magnetoresistance only develop inside the CDW phase, which is seen more clearly by taking the difference between data recorded in zero field and 13 T [see Fig. 1(d)]. The magneto-Seebeck response $\Delta S_{xx} = S_{xx}(13 \text{ T}) - S_{xx}(0 \text{ T})$ is practically zero above T_{CDW} within our measurement uncertainties. The magnitude of ΔS_{xx} grows gradually inside the CDW, reaching a maximum around 20 K, which drops rapidly to zero approaching T_c. The magnetoresistance $\Delta\rho_{xx} = \rho_{xx}(13 \text{ T}) - \rho_{xx}(0 \text{ T})$ remains finite but nearly temperature-independent above T_{CDW}. It rises gradually by entering the CDW phase and eventually saturates below 10 K.

Figure 2 presents more details on the magneto-Seebeck $MS = [S_{xx}(B) - S_{xx}(0)]/S_{xx}(0)$ and magnetoresistance $MR = [\rho_{xx}(B) - \rho_{xx}(0)]/\rho_{xx}(0)$ measured at various temperatures. Clear quantum oscillations (QOs) are seen both in Seebeck and resistivity channels below 30 K, as shown in Figs. 2(a) and 2(c). The oscillatory component of MS as a function of $1/B$ is displayed in Fig. 2(b), by subtracting a polynomial background from 2 to 12 T. The fast Fourier transform (FFT) analysis of the oscillations is presented in Fig. 2(d). Four frequencies can be identified with $F_1 = 18$,

$F_2 = 28$, $F_3 = 72$ and $F_4 = 88$ T, which are consistent with earlier reports extracted from QOs in magnetoresistance [21,27]. We note that, much higher frequency up to $\sim$2000 T was observed in Shubnikov–de Haas oscillations [21], which is not evident in our data. Using the Onsager relation $F = (\hbar/2\pi e)A_F$, we can estimate the extremal area A_F of the Fermi surfaces with the frequency F obtained in Fig. 2(d). The obtained values are very small, which only occupy 0.11%, 0.18%, 0.45%, 0.56% of the first BZ size in the $k_x - k_y$ plane (a-axis lattice parameter: $a = 5.4949$ Å [4]), for F_1, F_2, F_3, and F_4, respectively. The effective mass (m^*) can be estimated by fitting the temperature dependence of the FFT peak amplitude $a_i(T)$ for each frequency $F_i(i = 1 - 4)$, using the Lifshitz-Kosevich approximation $a_i(T) \approx X/(\sinh X)$ with $X = 14.69 m^* T/B$. The magnetic field $B(= 7.25$ T in our case) is typically taken as the average value of the field range used for FFT analysis. As shown in the inset of Fig. 2(d), the obtained values of m^* for all frequencies are very small, suggesting contribution from the Dirac bands in the vicinity of the M point [21].

To further explore the multiband effect, the Hall resistivity (ρ_{yx}) measured at various temperatures is displayed in Fig. 3. The Hall resistivity is dominated by electronlike carriers
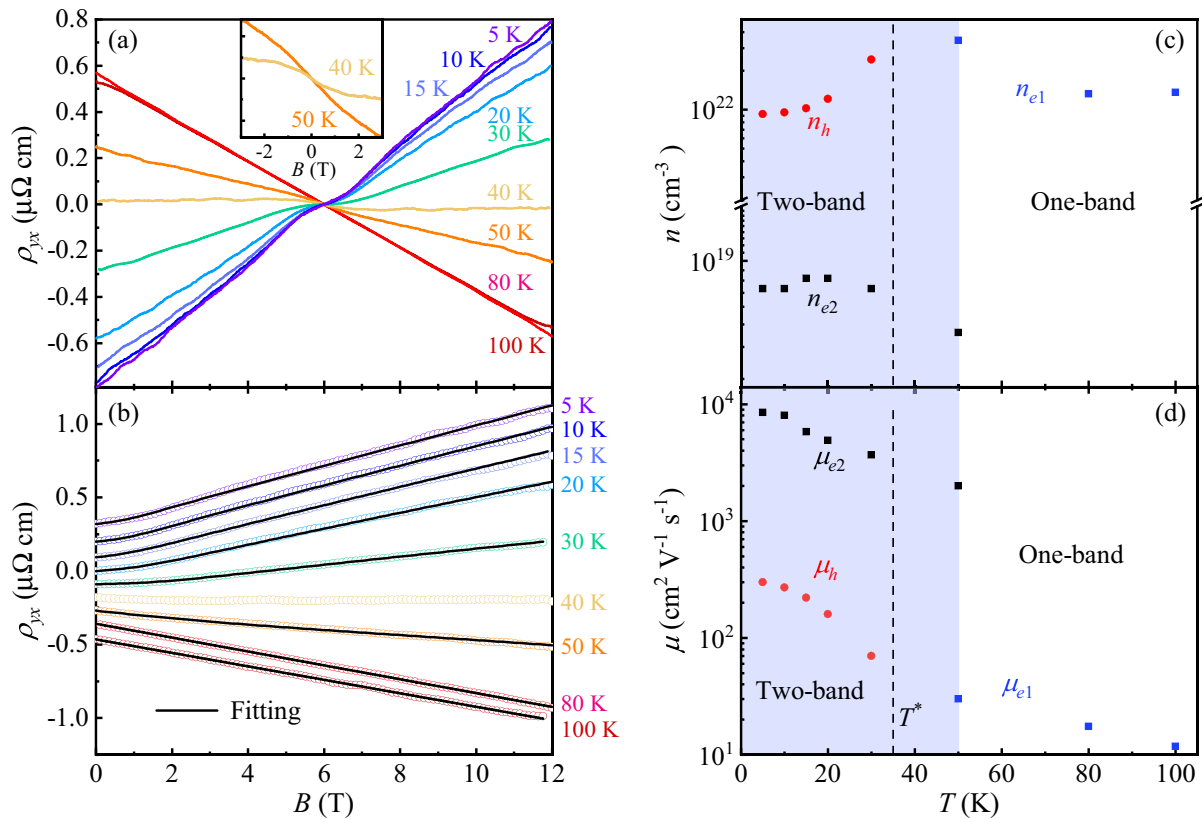
FIG. 3. (a) The Hall effect recorded at different temperatures using $B \parallel c$. (b) Two-band fitting (black lines) of the Hall resistivity ρ_{yx}. Curves have been shifted vertically for clarity. (c), (d) Estimated carrier density and mobility of each band from the analysis shown in (b). The inset in (a) shows an enlarged view of the nonlinear Hall resistivity at 40 and 50 K.

above 80 K, resulting in a linear $\rho_{yx}(B)$ with a negative slope [see Figs. 3(a) and 3(b)]. Sublinear effects develop below 50 K, which are seen more clearly in the inset of Fig. 3(a). Signatures of AHE are less evident compared with those reported earlier [26–28]. As suggested by Zheng *et al.*, slight variation of the Fermi level can significantly affect the appearance of AHE [28], which possibly explains the negligible AHE signal observed here. Further cooling leads to a sign change in ρ_{yx}, which becomes positive below 40 K. Similar sign change at $T^* \sim 35$ K has also been reported earlier [27], and also appears in $K_{1-x}V_3Sb_5$ [26] and RbV_3Sb_5 [7]. To model the nonlinear Hall resistivity, we used a two-band approximation [38]:

$$\rho_{yx}(B) = \frac{B}{e} \frac{\left(n_h\mu_h^2 - n_e\mu_e^2\right) + \mu_h^2\mu_e^2 B^2(n_h - n_e)}{(n_h\mu_h + n_e\mu_e)^2 + \mu_h^2\mu_e^2 B^2(n_h - n_e)^2}, \quad (3)$$

with the constraint of zero field conductivity $\sigma_{xx} = n_h e\mu_h + n_e e\mu_e$. As shown in Fig. 3(b), the nonlinear $\rho_{yx}(B)$ curves below 50 K can be described by this two-band fitting. At the verge of sign switching around 40 K, the attempt of fitting using the simple two-band model was not successful. The extracted density and mobility of each band are presented in Figs. 3(c) and 3(d). Above 50 K, the Hall resistivity is dominated by a single electron band ($e1$) with a carrier density $n_{e1} \sim 10^{22}$ cm^{-3}, and mobility $\mu_{e1} \sim 10$ cm^2 V^{-1}s^{-1}. A second electron band ($e2$) appears below 50 K, whose density is much lower ($n_{e2} \sim 10^{18}$ cm^{-3}), but possessing much

higher mobility ($\mu_{e2} \sim 10^3$ cm^2 V^{-1}s^{-1}), compared with those of $e1$. The $e1$ electron band disappears below 40 K, and a hole band (h) shows up with similar density but higher mobility ($\mu_h \sim 10^2$ cm^2 V^{-1}s^{-1}) compared with those in the $e1$ band, which leads to the sign change in ρ_{yx}. The much higher mobility of the $e2$ electron band ensures the negative sign in thermopower all the way down to about 7 K [see Fig. 1(b)], despite the larger concentration of the hole band.

Similarly as shown in Fig. 4(a), the Nernst signal, $S_{yx} = E_y/\nabla_x T$, scales linearly with B above 50 K, and becomes sublinear at lower temperatures. Notably, instead of switching sign around 30–40 K in Hall resistivity, the Nernst signal reaches maximum at this temperature region. In Fig. 4(b), we directly compare the Hall resistivity and the Nernst coefficient ($\nu = S_{yx}/B_z$) measured at $B_z = 12$ T. The Nernst coefficient, grows gradually upon cooling and peaks at $T^* \sim 35$ K. Further cooling causes a rapid drop in ν, which changes sign below 20 K. The Hall resistivity ρ_{yx}, on the other hand, switches sign around T^*. Similar effects, i.e., the Nernst coefficient peaks at the temperature where the Hall coefficient switches sign, has been observed in the CDW phase of $2H$-NbSe$_2$ superconductor, which was attributed to the ambipolar transport of compensated electron and hole bands [39]. The same physics is very likely happening here for CsV$_3$Sb$_5$. The compensation can happen at the switching point between the $e1$ electron and the h hole bands at T^*.
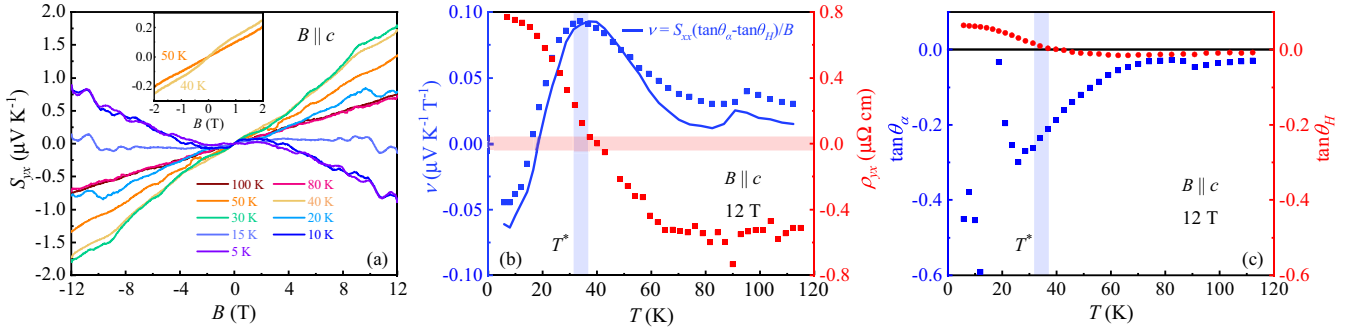
FIG. 4. (a) The Nernst effect measured at various temperatures with $B \parallel c$. Inset: Enlarged view of the nonlinear response at 40 and 50 K. (b) Comparison of the Nernst coefficient $\nu = S_{yx}/B_z$ and Hall resistivity measured at $B_z = 12$ T. The temperature $T^* \sim 35$ K, at which ν reaches maximum and ρ_{yx} switches sign, is marked out by blue and red shaded stripes. (c) The temperature dependence of two Hall-like angles θ_H and θ_α. The solid blue line in (b) is a calculation of the Nernst coefficient $\nu = S_{xx}(\tan\theta_\alpha - \tan\theta_H)/B_z$ according to Eq. (4).

As shown by Wang *et al.* [40], the Nernst signal can be expressed as

$$S_{yx} = S_{xx}\left(\frac{\alpha_{yx}}{\alpha_{xx}} - \frac{\sigma_{yx}}{\sigma_{xx}}\right) = S_{xx}(\tan\theta_\alpha - \tan\theta_H)$$

$$= \frac{\pi^2}{3}\frac{k_B^2 T}{e}\left(\frac{\partial \tan\theta_H}{\partial E}\right)\bigg|_{E_F}, \qquad (4)$$

assuming negligible transverse thermal gradient $\nabla_y T$. Here, α_{ij} ($i, j = x, y$) and σ_{ij} are components of the Peltier conductivity $\overline{\alpha}$ and electrical conductivity $\overline{\sigma}$ tensors, respectively. The Hall angle is defined as $\theta_H = \frac{\sigma_{yx}}{\sigma_{xx}}$, and the other Hall-like angle is $\theta_\alpha = \frac{\alpha_{yx}}{\alpha_{xx}}$. For a one-band metal, if the conductivity $\overline{\sigma}$ is energy-independent, i.e., $(\frac{\partial \tan\theta_H}{\partial E})|_{E_F} = 0$, the two angles θ_H and θ_α cancel out with each other (Sondheimer cancellation), leading to a vanishing Nernst signal [40], as found in typical metals [41]. Such a cancellation can be avoided in a multiband system with different types of carriers. For simplicity, we consider a two-band system consisting of electronlike and holelike bands. The Nernst signal in Eq. (4) now reads [39,41]:

$$S_{yx} = S_{xx}\left(\frac{\alpha_{yx}^h + \alpha_{yx}^e}{\alpha_{xx}^h + \alpha_{xx}^e} - \frac{\sigma_{yx}^h + \sigma_{yx}^e}{\sigma_{xx}^h + \sigma_{xx}^e}\right), \qquad (5)$$

with the h and e superscripts representing holelike and electronlike pockets, respectively. In general, the Sondheimer cancellation for each band does not lead to zero value in the net Nernst signal shown in Eq. (5), since the signs of α_{ij} and σ_{ij} now depend on the type of carriers [39,41]. In the extreme case of compensated electronlike and holelike bands, $\sigma_{yx}^h = -\sigma_{yx}^e$, whereas α_{yx}^h and α_{yx}^e have the same sign and contribute additively to the Nernst effect, resulting in an enhanced S_{yx} as seen in Eq. (5). Note that α_{xx}^h and α_{xx}^e also have opposite signs, but do not cancel out generally. Such a kind of enhanced Nernst effect is typically observed in compensated semiconductors, which is called the ambipolar Nernst effect [42]. Examples of ambipolar Nernst effect are rarely found in metals. The CsV$_3$Sb$_5$ Kagome material may represent another prime metallic system to study the ambipolar effects, in addition to 2H-NbSe$_2$ [39].

Figure 4(c) compares the two Hall-like angles θ_H and θ_α. The components of the Peltier conductivity can be evaluated using $\alpha_{yx} = (\rho_{xx}S_{yx} - \rho_{yx}S_{xx})/(\rho_{xx}^2 + \rho_{yx}^2)$, and $\alpha_{xx} = (\rho_{yx}S_{yx} + \rho_{xx}S_{xx})/(\rho_{xx}^2 + \rho_{yx}^2)$ [43,44]. Here, the isotropic diagonal components $\rho_{xx} = \rho_{yy}$ and $S_{xx} = S_{yy}$ are assumed. One can see that the difference between θ_H and θ_α increases steadily upon cooling, which reaches a local maximum around 30 K. Further cooling leads to rapid decrease in the magnitude of $|\theta_\alpha - \theta_H|$, causing a decreasing Nernst signal as shown in Fig. 4(b). Below 20 K, the separation between θ_H and θ_α recovers to larger values. However, as shown in Fig. 1(b), the thermopower S_{xx} changes sign around 20 K in a magnetic field of 13 T, which also leads to a sign switching in the Nernst effect according to Eq. (4). The solid blue line in Fig. 4(b) shows an estimation of the Nernst signal using Eq. (4), which recovers the experimental data quantitatively well. These results suggest that the Nernst peak around T^* is mainly originated from the large deviations between θ_H and θ_α due to the ambipolar transport nature, similar to that in 2H-NbSe$_2$ [39].

In summary, we have investigated magneto-Seebeck and Nernst effect in CsV$_3$Sb$_5$. The transport in the CDW phase is dominated by multiband electronic structure as evidenced by sign switching effects in thermopower and Hall resistivity, nonlinear Hall resistivity, and Nernst effect. The ambipolar flow of different carriers produces large Nernst signal, which peaks at the sign change temperature of the Hall coefficient, suggesting the existence of nearly compensated bands. These findings point to the important role played by the multiband nature in the transport properties of CsV$_3$Sb$_5$, and suggest that CsV$_3$Sb$_5$ is another prominent metallic system to investigate the ambipolar effects.

Note added in proof. While this article was under review, two other Seebeck and Nernst studies appeared on arXiv [45,46], which agree qualitatively with our results.

[1] R. M. Fernandes, P. P. Orth, and J. Schmalian, Annu. Rev. Condens. Matter Phys. **10**, 133 (2019).

[2] Y. Tokura, K. Yasuda, and A. Tsukazaki, Nat. Rev. Phys. **1**, 126 (2019).

[3] M. Sato and Y. Ando, Rep. Prog. Phys. **80**, 076501 (2017).

[4] B. R. Ortiz, L. C. Gomes, J. R. Morey, M. Winiarski, M. Bordelon, J. S. Mangum, I. W. Oswald, J. A. Rodriguez-Rivera, J. R. Neilson, S. D. Wilson, E. Ertekin, T. M. McQueen, and E. S. Toberer, Phys. Rev. Materials **3**, 094407 (2019).

[5] B. R. Ortiz, S. M. L. Teicher, Y. Hu, J. L. Zuo, P. M. Sarte, E. C. Schueller, A. M. Abeykoon, M. J. Krogstad, S. Rosenkranz, R. Osborn, R. Seshadri, L. Balents, J. He, and S. D. Wilson, Phys. Rev. Lett. **125**, 247002 (2020).

[6] B. R. Ortiz, P. M. Sarte, E. M. Kenney, M. J. Graf, S. M. Teicher, R. Seshadri, and S. D. Wilson, Phys. Rev. Materials **5**, 034801 (2021).

[7] Q. Yin, Z. Tu, C. Gong, Y. Fu, S. Yan, and H. Lei, Chin. Phys. Lett. **38**, 037403 (2021).

[8] Y. X. Jiang, J. X. Yin, M. M. Denner, N. Shumiya, B. R. Ortiz, G. Xu, Z. Guguchia, J. He, M. S. Hossain, X. Liu, J. Ruff, L. Kautzsch, S. S. Zhang, G. Chang, I. Belopolski, Q. Zhang, T. A. Cochran, D. Multer, M. Litskevich, Z. J. Cheng *et al.*, Nat. Mater. **20**, 1353 (2021).

[9] Z. Liang, X. Hou, F. Zhang, W. Ma, P. Wu, Z. Zhang, F. Yu, J.-J. Ying, K. Jiang, L. Shan, Z. Wang, and X.-H. Chen, Phys. Rev. X **11**, 031026 (2021).

[10] H. Zhao, H. Li, B. R. Ortiz, S. M. L. Teicher, T. Park, M. Ye, Z. Wang, L. Balents, S. D. Wilson, and I. Zeljkovic, Nature **599**, 216 (2021).

[11] H. Chen, H. Yang, B. Hu, Z. Zhao, J. Yuan, Y. Xing, G. Qian, Z. Huang, G. Li, Y. Ye, S. Ma, S. Ni, H. Zhang, Q. Yin, C. Gong, Z. Tu, H. Lei, H. Tan, S. Zhou, C. Shen *et al.*, Nature **599**, 222 (2021).

[12] H.-S. Xu, Y.-J. Yan, R. Yin, W. Xia, S. Fang, Z. Chen, Y. Li, W. Yang, Y. Guo, and D.-L. Feng, Phys. Rev. Lett. **127**, 187004 (2021).

[13] H. Li, H. Zhao, B. R. Ortiz, T. Park, M. Ye, L. Balents, Z. Wang, S. D. Wilson, and I. Zeljkovic, arXiv:2104.08209.

[14] N. Shumiya, M. S. Hossain, J.-X. Yin, Y.-X. Jiang, B. R. Ortiz, H. Liu, Y. Shi, Q. Yin, H. Lei, S. S. Zhang, G. Chang, Q. Zhang, T. A. Cochran, D. Multer, M. Litskevich, Z.-J. Cheng, X. P. Yang, Z. Guguchia, S. D. Wilson, and M. Z. Hasan, Phys. Rev. B **104**, 035131 (2021).

[15] Z. Wang, Y.-X. Jiang, J.-X. Yin, Y. Li, G.-Y. Wang, H.-L. Huang, S. Shao, J. Liu, P. Zhu, N. Shumiya, M. S. Hossain, H. Liu, Y. Shi, J. Duan, X. Li, G. Chang, P. Dai, Z. Ye, G. Xu, Y. Wang *et al.*, Phys. Rev. B **104**, 075148 (2021).

[16] Y. Xiang, Q. Li, Y. Li, W. Xie, H. Yang, Z. Wang, Y. Yao, and H.-H. Wen, Nat. Commun. **12**, 6767 (2021).

[17] H. Li, T. T. Zhang, T. Yilmaz, Y. Y. Pai, C. E. Marvinney, A. Said, Q. W. Yin, C. S. Gong, Z. J. Tu, E. Vescovo, C. S. Nelson, R. G. Moore, S. Murakami, H. C. Lei, H. N. Lee, B. J. Lawrie, and H. Miao, Phys. Rev. X **11**, 031050 (2021).

[18] K. Nakayama, Y. Li, T. Kato, M. Liu, Z. Wang, T. Takahashi, Y. Yao, and T. Sato, Phys. Rev. B **104**, L161112 (2021).

[19] Z. Wang, S. Ma, Y. Zhang, H. Yang, Z. Zhao, Y. Ou, Y. Zhu, S. Ni, Z. Lu, H. Chen, K. Jiang, L. Yu, Y. Zhang, X. Dong, J. Hu, H.-J. Gao, and Z. Zhao, arXiv:2012.05898.

[20] Z. Liu, N. Zhao, Q. Yin, C. Gong, Z. Tu, M. Li, W. Song, Z. Liu, D. Shen, Y. Huang, K. Liu, H. Lei, and S. Wang, Phys. Rev. X **11**, 041010 (2021).

[21] B. R. Ortiz, S. M. L. Teicher, L. Kautzsch, P. M. Sarte, N. Ratcliffe, J. Harter, J. P. C. Ruff, R. Seshadri, and S. D. Wilson, Phys. Rev. X **11**, 041030 (2021).

[22] Y. Hu, S. M. L. Teicher, B. R. Ortiz, Y. Luo, S. Peng, L. Huai, J. Z. Ma, N. C. Plumb, S. D. Wilson, J. F. He, and M. Shi, arXiv:2104.12725.

[23] K. Jiang, T. Wu, J.-X. Yin, Z. Wang, M. Z. Hasan, S. D. Wilson, X. Chen, and J. Hu, arXiv:2109.10809.

[24] H. Tan, Y. Liu, Z. Wang, and B. Yan, Phys. Rev. Lett. **127**, 046401 (2021).

[25] J. Zhao, W. Wu, Y. Wang, and S. A. Yang, Phys. Rev. B **103**, L241117 (2021).

[26] S. Y. Yang, Y. Wang, B. R. Ortiz, D. Liu, J. Gayles, E. Derunova, R. Gonzalez-Hernandez, L. Šmejkal, Y. Chen, S. S. Parkin, S. D. Wilson, E. S. Toberer, T. McQueen, and M. N. Ali, Sci. Adv. **6**, eabb6003 (2020).

[27] F. H. Yu, T. Wu, Z. Y. Wang, B. Lei, W. Z. Zhuo, J. J. Ying, and X. H. Chen, Phys. Rev. B **104**, L041103 (2021).

[28] G. Zheng, Z. Chen, C. Tan, M. Wang, X. Zhu, S. Albarakati, M. Algarni, J. Partridge, L. Farrar, J. Zhou, W. Ning, M. Tian, M. S. Fuhrer, and L. Wang, arXiv:2109.12588.

[29] E. M. Kenney, B. R. Ortiz, C. Wang, S. D. Wilson, and M. J. Graf, J. Phys.: Condens. Matter **33**, 235801 (2021).

[30] C. Mielke, D. Das, J. X. Yin, H. Liu, R. Gupta, C. N. Wang, Y. X. Jiang, M. Medarde, X. Wu, H. C. Lei, J. J. Chang, P. Dai, Q. Si, H. Miao, R. Thomale, T. Neupert, Y. Shi, R. Khasanov, M. Z. Hasan, H. Luetkens *et al.*, arXiv:2106.13443.

[31] L. Yu, C. Wang, Y. Zhang, M. Sander, S. Ni, Z. Lu, S. Ma, Z. Wang, Z. Zhao, H. Chen, K. Jiang, Y. Zhang, H. Yang, F. Zhou, X. Dong, S. L. Johnson, M. J. Graf, J. Hu, H.-J. Gao, and Z. Zhao, arXiv:2107.10714.

[32] X. Feng, K. Jiang, Z. Wang, and J. Hu, Sci. Bull. **66**, 1384 (2021).

[33] C. C. Zhao, L. S. Wang, W. Xia, Q. W. Yin, J. M. Ni, Y. Y. Huang, C. P. Tu, Z. C. Tao, Z. J. Tu, C. S. Gong, H. C. Lei, Y. F. Guo, X. F. Yang, and S. Y. Li, arXiv:2102.08356.

[34] R. Barnard, *Thermoelectricity in Metals and Alloys* (Taylor & Francis Ltd, London, 1972), p. 136.

[35] See Supplemental Material at http://link.aps.org/supplemental/10.1103/PhysRevB.104.L180508 for further experimental details.

[36] N. Mott and H. Jones, *The Theory of the Properties of Metals and Alloys* (Clarendon Press, Oxford, 1936).

[37] K. Behnia, D. Jaccard, and J. Flouquet, J. Phys.: Condens. Matter **16**, 5187 (2004).

[38] R. G. Chambers, Proc. Phys. Soc. London, Ser. A **65**, 903 (1952).

[39] R. Bel, K. Behnia, and H. Berger, Phys. Rev. Lett. **91**, 066602 (2003).

[40] Y. Wang, Z. A. Xu, T. Kakeshita, S. Uchida, S. Ono, Y. Ando, and N. P. Ong, Phys. Rev. B **64**, 224519 (2001).

[41] K. Behnia, J. Phys.: Condens. Matter **21**, 113101 (2009).

[42] R. T. Delves, Rep. Prog. Phys. **28**, 249 (1965).

[43] X. Li, L. Xu, L. Ding, J. Wang, M. Shen, X. Lu, Z. Zhu, and K. Behnia, Phys. Rev. Lett. **119**, 056601 (2017).

[44] H. Yang, W. You, J. Wang, J. Huang, C. Xi, X. Xu, C. Cao, M. Tian, Z.-A. Xu, J. Dai, and Y. Li, Phys. Rev. Materials **4**, 024202 (2020).

[45] D. Chen, B. He, M. Yao, Y. Pan, H. Lin, W. Schnelle, Y. Sun, J. Gooth, L. Taillefer, and C. Felser, arXiv:2110.13085.

[46] X. Zhou, H. Liu, W. Wu, K. Jiang, Y. Shi, Z. Li, Y. Sui, J. Hu, and J. Luo, arXiv:2111.00727.